Wave Selection Problems in the Presence of a Bottleneck

Jonathan Ward[1], R. Eddie Wilson[1], and Peter Berg[2]

[1] University of Bristol, Department of Engineering Mathematics, Bristol BS8 1TR
[2] UOIT, Faculty of Science, Oshawa, ON, L1H 7K4, Canada

Abstract. The Optimal–Velocity (OV) model is posed on an inhomogeneous ring–road and the consequent spatial traffic patterns are described and analysed. Parameters are chosen throughout for which all uniform flows are linearly stable, and a simple model for a bottleneck is used in which the OV function is scaled down on a subsection of the road. The large-time behaviour of this system is stationary and it is shown that there are three types of macroscopic traffic pattern, each consisting of plateaus joined together by sharp fronts. These patterns solve simple flow and density balances, which in some cases have non-unique solutions. It is shown how the theory of characteristics for the classical Lighthill-Whitham PDE model may be used to explain qualitatively which solutions the OV model selects. However, fine details of the OV model solution structure may only be explained by higher order PDE modelling.

1 Introduction

The aim of this paper is to understand the steady state wave profiles that emerge in car-following models in the presence of spatial inhomogeneity. We simulate traffic with the Optimal Velocity model [1], posed on a ring-road that is made inhomogeneous by adding a simple model for a bottleneck, in which the Optimal Velocity function is reduced by a constant factor for some portion of the road. The surprise in this paper is that such a simple model set-up can display non-trivial solution structure.

The modelling of traffic flow can be understood at two distinct levels: microscopically, whereby each vehicle is considered individually, and macroscopically whereby traffic is considered as a continuous fluid. The simple discrete model that we consider here develops stable stationary patterns as $t \to \infty$, which can be understood by drawing parallels with continuum models.

The paper is set out as follows. In Sect. 2, we describe the OV model set-up that we use for the remainder of this paper, including precise details of how the spatial inhomogeneity is applied. Then in Sect. 3, we outline our numerical simulation and coarse-graining procedure, and we show results of three numerical experiments with qualitatively different solution structure as $t \to \infty$ (see Fig. 1). Sections 4 and 5 analyse these experiments using classical kinematic wave theory, firstly by analysing simple flow and density balances and then by using characteristic arguments to explain the wave selection principles. We calculate explicitly a phase diagram describing where the different solution types occur. Finally in Sect. 6, we conclude and indicate the success and failures of higher order continuum models in explaining the fine details of the solution structure.

2 Problem Set-Up

We consider the traffic patterns formed by a large number N of identical vehicles driving on a unidirectional single-lane ring-road of length L. Overtaking is not considered. Vehicles move in continuous space x and time t, and their displacements and velocities are labelled $x_n(t)$ and $v_n(t)$ respectively. We suppose that the direction of motion is in increasing x, and moreover that vehicles are labelled $n = 1, 2, \ldots, N$ in the downstream direction. For the vehicles' equations of motion, we adopt the well-known Optimal Velocity (OV) car-following model [1] for which

$$\dot{x}_n = v_n, \tag{1}$$

$$\dot{v}_n = \alpha \left\{ V(h_n; x) - v_n \right\}. \tag{2}$$

Here dot denotes differentiation with respect to time, and the rate constant $\alpha > 0$ is known as the sensitivity. The variable $h_n := x_{n+1} - x_n$ gives the headway, or gap to the vehicle in front, and loosely speaking the OV model describes the relaxation of traffic to a safe speed which is defined in terms of this gap. Note that under open boundary conditions one would need to prescribe the trajectory of the lead vehicle N, but on the ring-road we assume merely that it follows vehicle 1, so that $h_N = L + x_1 - x_N$.

The novelty in this paper is that we use an inhomogeneous OV function which takes the form

$$V(h_n; x) := \begin{cases} r_{\mathrm{B}} V(h_n), & 0 \le x \bmod L < \hat{L}L, \\ V(h_n), & \hat{L}L \le x \bmod L < L, \end{cases} \tag{3}$$

and which is thus scaled down by a reduction factor $0 < r_B < 1$ for a proportion $0 < \hat{L} < 1$ of the ring-road under consideration. (Note that for sake of brevity, the vehicles' displacements $x_n(t)$ are set-up as monotone increasing and unbounded, although henceforth, we interpret all displacements modulo L.)

In (3), V with a single argument denotes a spatially independent OV function, and for concreteness, we adopt the standard [1] S-shape

$$V(h) = \tanh(h - 2) + \tanh(2). \tag{4}$$

However, qualitatively similar results should be recovered by any V for which 1. $V(0) = 0$, 2. $V' \ge 0$ and 3. $V(h) \to V_{\max}$ as $h \to \infty$. The detailed structure of V is not important because throughout we choose $\alpha \ge 2\max V'$, so that all uniform flows are linearly stable. Consequently, the patterns that we observe are forced only by the spatial inhomogeneity and not by spontaneous flow breakdown effects.

3 Numerical Procedure and Simulation Results

We now supplement equations (1–3) with the uniformly spaced initial data

$$x_n = n h_* \qquad \text{and} \qquad v_n = V(h^*) \quad \text{for } n = 1, 2, \ldots, N. \tag{5}$$

Here $h^* := L/N$ is the mean spacing. Note that for the limiting (no bottleneck) cases where either $r_B = 1$ or $\hat{L} = 0$, (5) gives a uniform flow solution of (1–3) in which $x_n = nh_* + tV(h^*)$. However, in general we should expect the bottleneck to redistribute traffic. In order to investigate the resulting patterns, we solve the initial value problem (1–5) numerically using a standard fixed step fourth-order Runge-Kutta solver.

After some experimentation with the solver, we conclude that the traffic always settles down to a stationary profile as $t \to \infty$, although the transient processes can sometimes be very long. Here stationarity means that suitably defined macroscopic density and velocity variables become steady, although they are non-trivially dependent on space x, and consequently vehicles' motions are in fact periodic as $t \to \infty$, since as they drive around the ring-road, they move repeatedly through the spatial pattern and experience traffic jams, free-flowing regimes etc. Note however that if we chose smaller values of sensitivity α than presented here, so as to force the linear instability of a range uniform flows, then the macroscopic variables could also be non-trivially time-dependent as $t \to \infty$.

Taking into account the above discussion, the results that we display shortly show stationary macroscopic density profiles $\rho(x)$ rather than individual vehicle trajectories. The simplest way to relate microscopic and macroscopic variables is via $\rho(x_n, t) = 1/h_n(t)$, although it is well-known [2,3] that this relationship holds exactly only for entirely homogeneous situations. Therefore we use a coarse-grained [2] density

$$\rho(x,t) = \int_L \mathrm{d}x' \mathrm{d}t' \phi(x - x', t') \sum_n \delta(x_n(t') - x'), \tag{6}$$

with

$$\phi(x,t) = \frac{1}{2\pi\sigma^2} \exp(-x^2/2\sigma^2)\delta(t), \tag{7}$$

which is thus obtained from distributional point density by convolving with a Gaussian test function whose characteristic length scale σ is chosen large enough so as to smooth out individual vehicles but small enough so as to retain macroscopic features. A macroscopic flow variable $q(x,t)$ may be obtained in a similar way by coarse-graining the discrete velocity v_n, and then a coarse-grained velocity is given by $v(x,t) := q(x,t)/\rho(x,t)$. Note that since we are usually seeking a steady density, there are computational short-cuts and the cheapest procedure is to calculate $\rho(x)$ by coarse-graining in time the numerical trajectory of a single vehicle as it drives once around the ring-road.

We now give three examples of the eventual stationary profiles $\rho(x)$ which show how the structure changes as the mean headway h^* is varied. To simplify matters, all other parameters are held fixed as follows: $N = 100$ vehicles, bottleneck reduction factor $r_\mathrm{B} = 0.6$, bottleneck nondimensionalised length $\hat{L} = 0.25$ and sensitivity $\alpha = 2.0$. Later we consider how the qualitative solution structures change as functions of the three problem parameters $\rho_* := 1/h_*$, r_B and $\hat{L}$.

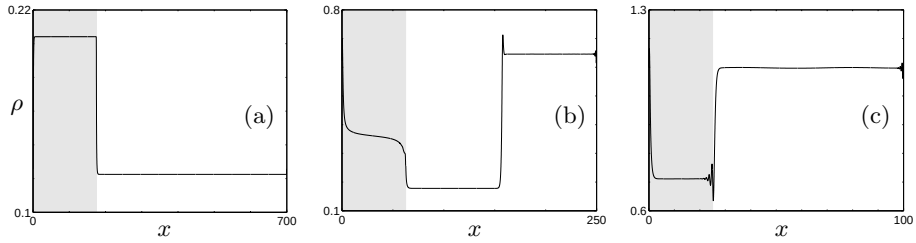

Fig. 1. Stationary $t \to \infty$ coarse-grained density profiles $\rho(x)$. The portions of solution profiles within the bottleneck are indicated by shading. (a) Light traffic $h_* = 7.0$ ($\rho_* = 0.142857$), see Example 1; (b) Medium traffic $h_* = 2.5$ ($\rho_* = 0.4$), see Example 3; (c) Heavy traffic $h_* = 1.0$ ($\rho_* = 1.0$), see Example 2

Example 1. We take $h_* = 7.0$ which corresponds to light traffic (large h_*, small ρ_*). See Fig. 1(a). The $t \to \infty$ steady density profile $\rho(x)$ adopts a two-plateau form, with an almost constant density $\rho_{\rm B}$ attained in the bottleneck and a lower (almost constant) density ρ_1 on the remainder of the loop. At each end of the bottleneck, the two density plateaus are joined by sharp, almost shock-like fronts.

Example 2. We take $h_* = 1.0$ which corresponds to heavy traffic. See Fig. 1(c). In a similar fashion to Example 1, $\rho(x)$ adopts a two-plateau form. However this time the bottleneck density $\rho_{\rm B}$ is less than the density ρ_1 on the unconstrained part of the loop. Like Example 1, there are also sharp, shock-like fronts at each end of the bottleneck, although here they have a more complicated oscillatory structure.

Example 3. We now take $h_* = 2.5$ which may be regarded as an intermediate case. See Fig. 1(b). In contrast to the two previous examples, $\rho(x)$ now has a three-plateau form. The density as before adopts an almost constant (but slightly S-shaped) profile $\rho \simeq \rho_{\rm B}$ within the bottleneck, with fronts at each end. Downstream of the bottleneck is a low density ρ_1 region, whereas upstream is a high density ρ_2 region, which may be thought of as a queue waiting to enter the bottleneck. There is thus an extra internal shock-like front in the unconstrained part of the loop, where the fast traffic that has come out of the bottleneck rejoins the queue to enter it. Unlike the other fronts we have encountered so far, that joining ρ_1 and ρ_2 is not locked on a discontinuity in the model; nevertheless, it is stationary.

Further simulation may be used to show how the Fig. 1 profiles are related to each other. If one starts with the Fig. 1(b) structure (Example 3) and decreases the mean headway (increases the mean density), then the queue upstream of the bottleneck grows in length until it reaches the downstream boundary of the bottleneck, and swamps the entire unconstrained part of the loop. At this point, the internal shock vanishes and the Fig. 1(c) structure is recovered. Conversely, if one starts with Fig. 1(b) and decreases the mean density, the queue upstream of the bottleneck shortens until it vanishes altogether. At that point, the internal

shock is absorbed into the upstream boundary of the bottleneck and the Fig. 1(a) structure is recovered.

4 Density and Flow Balances

We now begin an explanation of the structures seen in Section 3. Later we derive a phase diagram which predicts when each will occur. Since the observed structures resemble constant density plateaus separated by classical shocks, we attempt an explanation based on kinematic wave theory [6]. To this end, we introduce the fundamental (flow) diagram $Q(\rho) = \rho\hat{V}(\rho)$ where $\hat{V}(\rho) = V(1/\rho)$ is the continuum counterpart to the discrete OV function V. As is well-known, Q is usually a unimodal function. With choice (4), Q attains its maximum value $Q_{\max} \simeq 0.58$ at $\rho_{\max} \simeq 0.36$. In the bottleneck, the fundamental diagram Q is scaled by r_{B}.

Firstly we consider the two-plateau structures of Figs. 1(a) and (c). Since the fronts are sharp, negligibly few vehicles are contained within them at any one time. We may therefore approximate the density $\rho(x)$ with a piecewise-constant profile consisting of ρ_{B} within the bottleneck and ρ_1 in the unconstrained part of the loop. It thus follows that

$$\hat{L}\rho_{\mathrm{B}} + (1-\hat{L})\rho_1 = \rho_*, \tag{8}$$

$$Q(\rho_1) = r_{\mathrm{B}} Q(\rho_{\mathrm{B}}), \tag{9}$$

which describe respectively the conservation of vehicles and a flow balance (the latter is necessary since the observed profiles are stationary). Equations (8,9) are thus a pair of simultaneous equations to solve for ρ_1 and ρ_{B}, where the remaining parameters ρ_*, r_{B} and $\hat{L}$ are prescribed.

We must therefore examine the $(\rho_1, \rho_{\mathrm{B}})$ solution structure of (8,9) and this is achieved via Fig. 2. To see this, note that ρ_{B} may be eliminated from (8,9) to give

$$Q(\rho_1) = r_{\mathrm{B}} Q\left(\frac{\rho_* - (1-\hat{L})\rho_1}{\hat{L}}\right), \tag{10}$$

and the left and right hand sides of this equation are plotted against ρ_1 in Figs. 2(a-c)(i). Note alternatively that ρ_1 can be eliminated from (8,9) to give

$$r_{\mathrm{B}} Q(\rho_{\mathrm{B}}) = Q\left(\frac{\rho_* - \hat{L}\rho_{\mathrm{B}}}{1-\hat{L}}\right), \tag{11}$$

and as a cross-check, the left and right hand sides of this equation are plotted against ρ_{B} in Figs. 2(a-c)(ii). Further, parameters have been chosen so that the panels (a-c) correspond directly to panels (a-c) in Fig. 1. Firstly, the light traffic diagrams Figs. 2(a)(i,ii) indicate a unique $(\rho_1, \rho_{\mathrm{B}})$ solution pair and it may be shown that this is indeed corresponds to values obtained in Example 1.

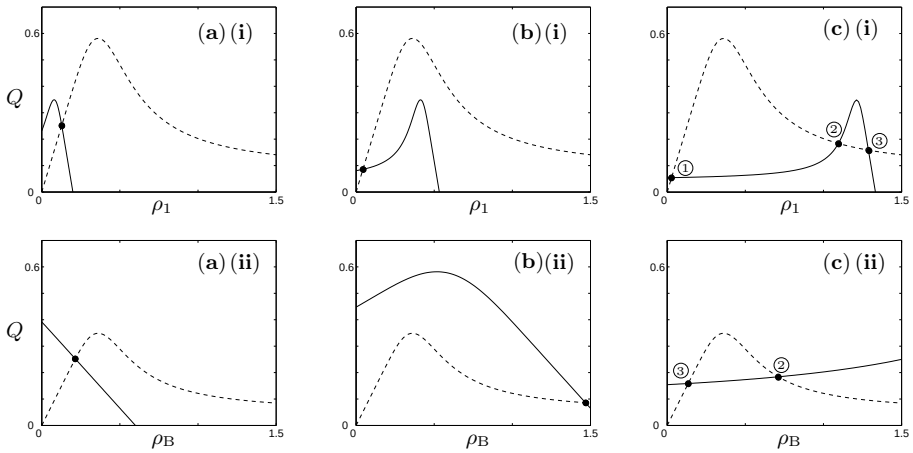

Fig. 2. Solution structure of (8,9). Panels (a-c) correspond directly to panels (a-c) in Fig. 1. Top row (i) indicates solutions of (10) and bottom row (ii) of the equivalent equation (11). The extra numbering in panels (c)(i,ii) allows the (ρ_1, ρ_B) solution pairs to be identified

However, in the heavy traffic diagrams Figs. 2(c)(i,ii), there are clearly three (ρ_1, ρ_B) solution pairs: what determines which pair is selected in the corresponding Example 2? Finally, in the intermediate case of Figs. 2(b)(i,ii), there is a unique (ρ_1, ρ_B) solution pair, however, the corresponding Example 3 selects instead a three-plateau structure. It now remains to identify extra principles which explain the solution selection in cases (b) (Example 3) and (c) (Example 2).

5 Wave Selection via Characteristics

We now use characteristic arguments from kinematic wave theory [6, Chap. 2] to explain the observed wave selection behaviour. We focus initially on Example 2 (heavy traffic), see Figs. 1(c) and Figs. 2(c)(i,ii), and then later we consider the three-plateau case.

We recall that in kinematic wave theory, characteristics are lines (or line segments) in the (x, t) plane on which density is conserved. Further, it is well-known that the local velocity of a characteristic with density ρ is given by $Q'(\rho)$. Consequently, characteristics propagate downstream in light traffic and upstream in heavy traffic. When characteristics converge, one obtains a classical shock, whereas when they diverge, one obtains a (non-stationary) expansion fan.

Figure 3 develops a characteristic analysis of the (ρ_1, ρ_B) solution pairs found in Fig. 2(c)(i,ii). The key point to note is that the solution pairs numbered 1 and 3 straddle $\rho = \rho_{\max}$ at which both the unconstrained $Q(\rho)$ and bottleneck $r_B Q(\rho)$ fundamental diagrams attain their maxima. These solution pairs can be disregarded, because the consequent density profiles would involve patterns of characteristics with both positive and negative slopes. This means that at

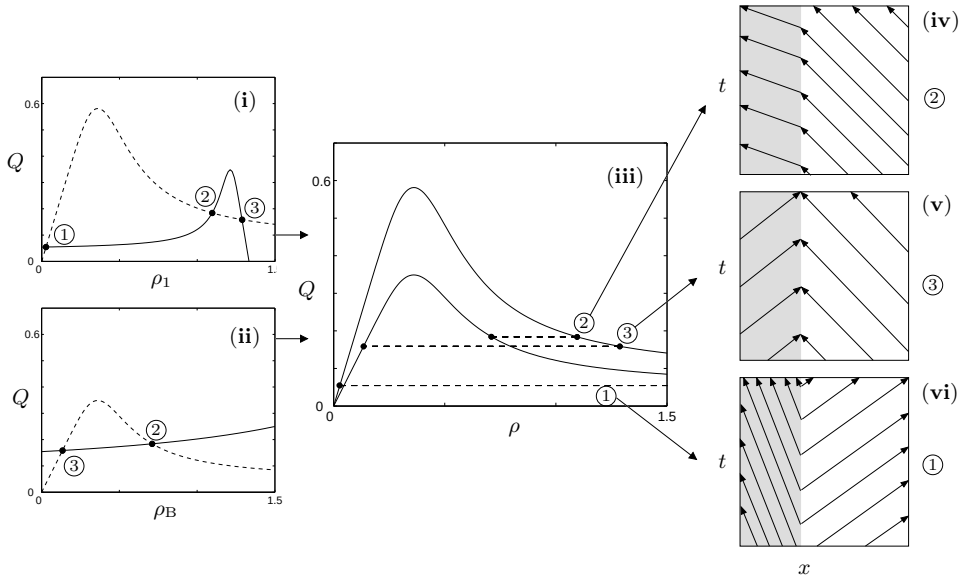

Fig. 3. Characteristic analysis for the (ρ_1, ρ_B) solution pairs from Figs. 2(c)(i,ii). Panel (iii) shows the location of solution pairs, joined by horizontal lines representing flow balance, on the fundamental diagrams Q and $r_B Q$. Characteristic pictures for each of the three root pairs are shown in panels (iv), (v) and (vi): the bottleneck is denoted by shading. Panels (v) and (vi) cannot give stationary profiles since they predict an expansion fan at the up- and down-stream ends of the bottleneck respectively. Hence solution pair 2 from panel (iv) is selected. Note that in panel (iii), this solution pair is non-straddling in the sense that both ρ_1 and ρ_B are the same side of the fundamental diagram maximum

either the upstream or downstream boundary of the bottleneck, there would necessarily be a non-stationary expansion fan which would not agree with the $t \to \infty$ stationary results.

In contrast, solution pair 2 is non-straddling and involves only characteristics with negative slopes, see Fig. 3 panel (iv). In this sketch, neither the upstream or downstream boundary of the bottleneck has a classical (compressive) shock. Rather, at each boundary the characteristics cross through the shock which is forced solely by the model discontinuity at that point. It may be shown that this solution agrees with that found by discrete simulation in Section 3 and moreover that it is a proper solution of the Lighthill-Whitham-Richards model in that it may be reached via the solution of the initial value problem [8].

We now turn our attention to the three-plateau case (Example 3, Fig. 1(b)), for which it may be shown that the analysis of Section 4 predicts a straddling, and hence invalid solution pair (ρ_1, ρ_B). The resolution is thus to approximate the density $\rho(x)$ by a piecewise-constant profile with three components: ρ_B (density in bottleneck) and ρ_1, ρ_2 (densities in unconstrained part of loop). The density

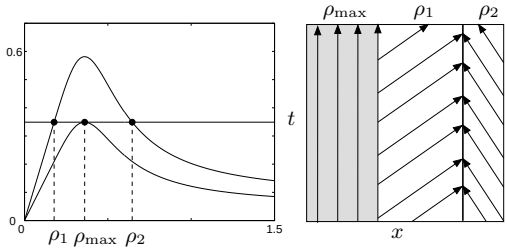

Fig. 4. Characteristic analysis for the three-plateau case: only the configuration shown with flow maximised in the bottleneck avoids expansion fans. Note that the characteristics inside the bottleneck have zero velocity and hence this structure is on the very boundary of becoming an expansion fan. The internal shock between ρ_1 and ρ_2 is classical since at it the characteristics converge

and flow balances thus yield respectively

$$\hat{L}\rho_{\mathrm{B}} + \beta(1-\hat{L})\rho_1 + (1-\beta)(1-\hat{L})\rho_2 = \rho_*, \tag{12}$$

$$Q(\rho_1) = Q(\rho_2) = r_{\mathrm{B}} Q(\rho_{\mathrm{B}}), \tag{13}$$

where $0 < \beta < 1$ parametrises the internal shock position separating ρ_1 and ρ_2. We thus have three equations, but four unknowns, namely β, ρ_1, ρ_2 and ρ_{B}, and we require extra information to fix a unique solution. By studying characteristic diagrams, it becomes clear that a solution without diverging characteristics (and hence non-stationary expansion fans) is only possible if

$$\rho_{\mathrm{B}} = \rho_{\max}, \tag{14}$$

i.e., if the flow inside the bottleneck is maximised. Further, when supplemented by (14), system (12,13) can be solved uniquely for ρ_1, ρ_2 and β, and it may be shown that this solution agrees with the discrete simulations. The characteristic structure is shown in Fig. 4. In particular, it involves non-standard waves at the up- and down-stream ends of the bottleneck. However it may be shown via the solution of the initial value problem that these are admissible solutions of the Lighthill-Whitham-Richards model [8].

We now turn our attention to the computation of a phase diagram. Since in the three-plateau case we have $\rho_{\mathrm{B}} = \rho_{\max}$, the values of ρ_* where solutions change from two plateau solutions to three plateau solutions can be calculated. At the thresholds, β is either 0 or 1 and $\rho_{\mathrm{B}} = \rho_{\max}$, thus eliminating ρ_1 or ρ_2 in (13) using (12), leaves only

$$r_{\mathrm{B}} Q(\rho_{\max}) = Q\left(\frac{\rho_* - \hat{L}\rho_{\max}}{1-\hat{L}}\right), \tag{15}$$

as a relation between the problem parameters that holds at the transition, see Fig. 5. In particular, we may partition the (ρ_*, r_{B}) plane according to whether the three-plateau solution occurs, or according to which type of two-plateau

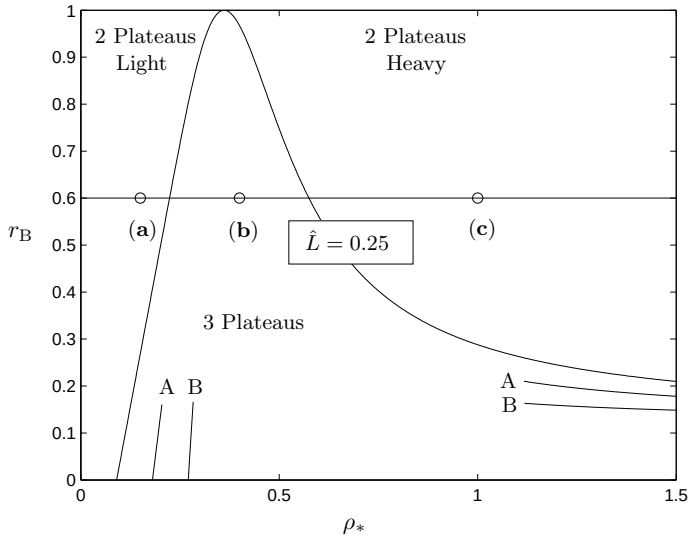

Fig. 5. Phase diagram derived from (15) for bottleneck length $\hat{L} = 0.25$. The points marked (a), (b), and (c) correspond to panels (a), (b) and (c) in Figs. 1 and 2. The line segments denoted A and B indicate to where the phase boundary would move for $\hat{L} = 0.5$ and $\hat{L} = 0.75$ respectively

solution occurs, and the boundary in this plane depends on $\hat{L}$ in a manner that we can determine explicitly. In particular, increasing the length of the bottleneck shrinks the domain where the three-plateau solution occurs.

6 Higher Order Modelling

We have shown how first order kinematic wave theory explains the principal qualitative features of the discrete simulation results presented in Fig. 1. This theory however is based on a piecewise-constant ansatz for the density profile $\rho(x)$, and does not explain, for example, the S-shaped profile in the bottleneck in Fig. 1(b), nor does it explain the internal structure of the shocks. To analyse these features, we should resort to higher order PDE approximations of the OV model [2,3]. Using the work of [7] as motivation, we use finite differences to obtain the spatial derivative of the coarse-grained density so that we may display numerical (ρ, ρ_x) phase portraits: see Figs. 6(a–c).

In each of these phase portraits, trajectories spend most time in the vicinity of fixed points which correspond to the constant density plateaus in Figs. 1(a–c). These fixed points are then linked via rapid transits across the phase portrait which describe the interior structure of the shocks. Note that in Figs. 6(a–c), the bottleneck boundaries are in fact 'mid-shock' and are denoted by small solid discs.

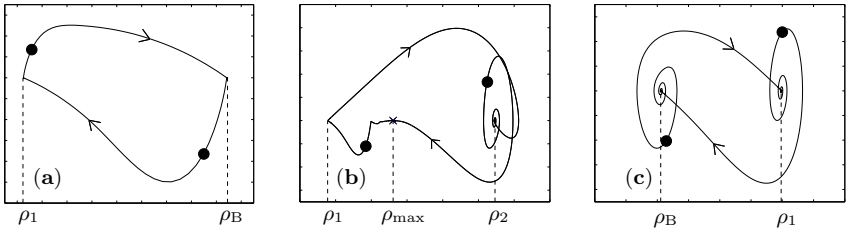

Fig. 6. Numerical (ρ,ρ_x) phase plots corresponding to Figs. 1(a–c). The discs mark the boundaries of the bottleneck. (a) Light traffic: heteroclinic cycle connecting $(\rho_1, 0)$ and $(\rho_B, 0)$. (b) Three plateau case: saddle at $(\rho_1, 0)$; saddle–node at $(\rho_B, 0)$ explaining S–shaped structure; complex fixed point at $(\rho_2, 0)$. (c) Heavy traffic: complex fixed points at $(\rho_1, 0)$ and $(\rho_2, 0)$

In the light traffic portrait Fig. 6(a), we observe a heteroclinic-cycle connecting saddle-like fixed points, which agrees with the analytical prediction of [7]. However, in the heavy traffic portrait Fig. 6(c), the numerical trajectory crosses itself, and we observe complicated fixed-points which resemble projections of Shilnikov points. The conclusion in this case is that the dynamics cannot be represented in two dimensions. In fact, one may show that the second-order theory [7] predicts a pair of stable node fixed points, and hence cannot produce the required connections. Instead, the solution seems to adopt a sharper profile which brings higher derivatives into play, and which thus permits the required connections in a higher dimensional phase space. In the three-plateau case Fig. 6(b), [7] predicts that the bottleneck fixed point is at saddle-node bifurcation, in the vicinity of which, trajectory behaviour is polynomial in x. This observation can be used to explain the S-shape bottleneck profile in Fig. 1(b).

Thus to sum up, from a simple model for a bottleneck on a loop, we have observed interesting, stationary wave patterns in the OV model as $t \to \infty$. These patterns consist generally of two or three plateaus separated by shock–like structures. We have built an understanding of these patterns using a PDE approach, principally by using first order kinematic wave theory. However, the fine details require higher order modelling with a momentum equation – this is work in progress.

References

1. M. Bando, K. Hasebe et al, Phys Rev. E **51**, 1035 (1995)
2. H.K. Lee, H. W. Lee, D. Kim, Phys. Rev E **64**, 056126 (2001)
3. P. Berg, A. Mason, A.W. Woods, Phys Rev. E **61**, 1056 (2000)
4. M.J. Lighthill, G.B. Whitham, Proc. R. Soc., A**229**, 317 (1955)
5. P.I. Richards, Operations Research, 4, 42-51 (1956)
6. G.B. Whitham: *Linear and Nonlinear Waves* (Wiley, New York, 1974)
7. R.E. Wilson and P. Berg, *Traffic and Granular Flow '01*, (Springer, Berlin, 2003)
8. W.L. Jin and H.M Zhang, Trans. Sci. **37(3)**, 294 (2003)